Editors' Suggestion

High-resolution spectroscopy of ^{162}Dy Rydberg levels

G. Ferioli,[1,2] P. Lombardi,[2,3] P. Sekhar,[1,2] E. Solé Cardona,[1,4] N. Preti,[1,2,4] C. Drevon,[1,2,4] N. Antolini,[2,4] L. Tanzi,[2,3] G. Modugno,[1,2,4] C. Gabbanini,[4] F. Robicheaux,[5,6] and A. Fioretti[2,4,*]

[1]*Dipartimento di Fisica e Astronomia, Università degli Studi di Firenze, Via G. Sansone 1, 50019 Sesto Fiorentino, Italy*
[2]*European Laboratory for Nonlinear Spectroscopy, Via N. Carrara 1, 50019 Sesto Fiorentino, Italy*
[3]*Istituto Nazionale di Ottica, Consiglio Nazionale delle Ricerche, Via N. Carrara 1, 50019 Sesto Fiorentino, Italy*
[4]*Istituto Nazionale di Ottica, Consiglio Nazionale delle Ricerche, Via Moruzzi 1, 56124 Pisa, Italy*
[5]*Department of Physics and Astronomy, Purdue University, West Lafayette, Indiana 47907, USA*
[6]*Purdue Quantum Science and Engineering Institute, Purdue University, West Lafayette, Indiana 47907, USA*

(Received 14 February 2026; accepted 20 May 2026; published 15 June 2026)

Highly excited Rydberg states of lanthanides are a promising, yet largely unexplored, playground for quantum studies. Here we report on the first high-resolution spectroscopy of ^{162}Dy obtained by two-color trap depletion spectroscopy in a magneto-optical trap. The absolute excitation frequency of over 700 states with effective principal quantum number $21 \leqslant n \leqslant 130$ is measured with an accuracy of 20 MHz. Most states are assigned to the eight different series converging to the first $4f^{10}(^5I_8)6s(^2S_{1/2})\,^6I_{17/2}$ ionization potential. This energy is measured at $E_{IP} = 47\,901.8265 \pm 0.0008$ cm^{-1}, improving the precision of the literature value by over an order of magnitude. A multichannel-quantum-defect-theory approach is used to benchmark and refine the assignments and to characterize six observed perturbing states belonging to higher ionization limits. These results pave the way for using dysprosium in Rydberg-based quantum architectures, leveraging the unique properties arising from its complex electronic structure. They also represent a compelling benchmark for *ab initio* calculations of open-shell atomic systems.

DOI: 10.1103/h4q7-6t3s

I. INTRODUCTION

Rydberg atoms are among the most promising platforms for quantum technologies [1], with wide-ranging applications in quantum information processing [2], quantum simulation [3], quantum metrology [4,5], and quantum optics [6,7].

While most experimental progress to date has relied on alkali-metal atoms, the richer electronic structure of alkaline-earth and alkaline-earth-like species, such as strontium and ytterbium, provides additional tools for cooling, trapping, and manipulating techniques [8–12]. These features have enabled new approaches, including erasure conversion protocols [13], midcircuit operations [14,15], and high-fidelity entangling gates [16–18].

Lanthanide atoms with an open submerged $4f$ shell, such as dysprosium and erbium, share many of these favorable properties, while also offering further or enhanced possibilities for quantum control. Similarly to Sr and Yb systems, the presence of multiple closed optical transitions with widely varying linewidths (ranging from megahertz-broad to ultranarrow clocklike transitions) has enabled single-atom trapping [19,20], high-fidelity imaging [19,21,22], cooling to the motional ground state [23], and precise internal-state manipulation [24,25].

At the same time, the large electronic angular momentum of the ground state gives rise to a manifold of long-lived Zeeman sublevels that can serve as a resource for high-dimensional qudit encoding [26,27], as originally proposed for holmium [28], or for the generation of nonclassical spin-cat states [29]. In addition, the large vector and tensor polarizabilities of the ground state enable the engineering of state-dependent trapping potentials over a broad range of wavelengths [30]. This capability allows controlled coupling between internal and motional degrees of freedom and creates an opportunity for improved motional gate schemes [31], with applications in the quantum simulation of fermionic systems [32].

Unlike Er [33], for which high-resolution Rydberg spectroscopy has recently become available, spectroscopic information on Rydberg states of Dy remains relatively limited. Earlier investigations were primarily based on multiphoton resonance ionization spectroscopy [34], which did not provide the level of precision now required for Rydberg-based quantum science applications. Here we present the first high-resolution spectroscopic survey of Rydberg states in ^{162}Dy, detecting more than 700 spectral lines with a typical accuracy of 20 MHz. We further determine the ionization potential with an order-of-magnitude improvement in precision over earlier measurements. By analyzing the observed perturbations, we identify the character of the main Rydberg series and benchmark our assignments using multichannel quantum-defect theory (MQDT).

This article is organized as follows. In Sec. II we describe the experimental setup and spectroscopy methods. In Sec. III we present the spectroscopic results, including the determination of the ionization potential E_{IP} and the assignment of the most relevant Rydberg series. In Sec. IV we outline the MQDT model used to fit the data. In Sec. V we discuss the information extracted from the amplitudes of the depletion

*Contact author: andrea.fioretti@ino.cnr.it

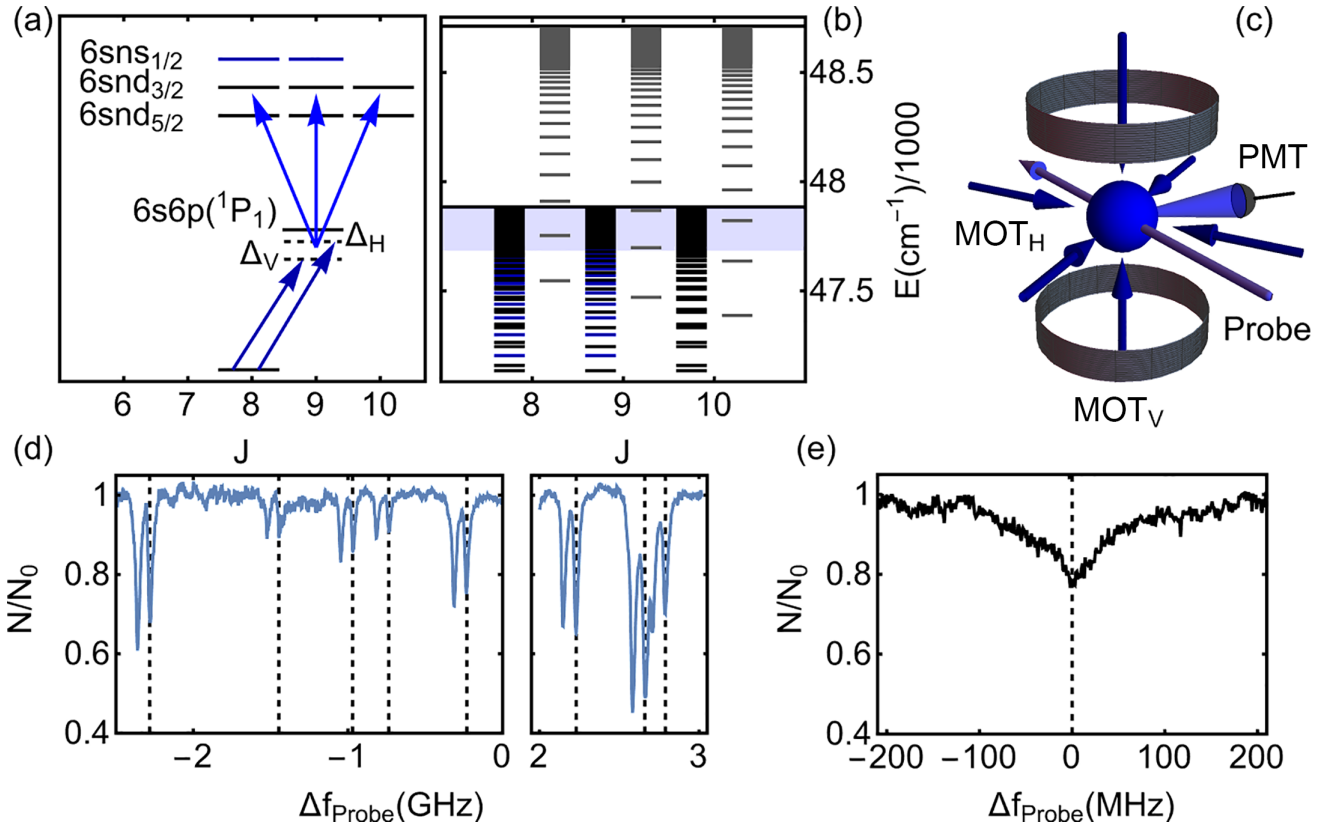

FIG. 1. (a) Scheme of two-photon excitation to the Rydberg levels. The first photon, nearly resonant with the intermediate $4f^{10}(^5I_8)6s6p(^1P_1^\circ)\,^5K_9$, $J = 9$ level, corresponds to the transition used for MOT operation. The two arrows indicate the two different excitation pathways employed, characterized by different detunings Δ_H and Δ_V (see the text for details). The three arrows originating from the intermediate state represent dipole-allowed transitions to states with s and d character and total angular momenta $J = 8, 9, 10$, resulting in the eight Rydberg series represented with their spectroscopic notation at the top of the panel. (b) Relevant Rydberg series. Black lines denote Rydberg levels converging to the first ionization threshold, i.e., the $4f^{10}(^5I_8)6s(^2S_{1/2})\,^6I_{17/2}$ ground state of the ion, while gray lines correspond to those associated with the second ionization threshold, i.e., the $4f^{10}(^5I_8)6s(^2S_{1/2})\,^6I_{15/2}$ first excited ionic state. The blue shaded area indicates the range of frequencies we explored. In (a) and (b) the Rydberg levels converging to the first ionization threshold with ns character are represented in blue, while the the nd are black. In (a) the energy difference between levels is not to scale. (c) Sketch of the core of the experimental platform. The two lasers used to operate the MOT are labeled Mot$_V$ and Mot$_H$, respectively. The laser exciting the atoms to the Rydberg states is labeled Probe, and the MOT fluorescence is detected by a photomultiplier tube (PMT). (d) Typical spectroscopic signal for $n = 90$. Over a frequency span of approximately 6 GHz, eight distinct features corresponding to the expected transitions are clearly visible and marked by vertical dashed lines. Each feature exhibits a doublet structure arising from the two different MOT laser frequencies (see the text for details). Here $\Delta f_{\text{Probe}} = 0$ corresponds to 1435.657 500(20) THz. (e) Example of a singlet transition signal.

signals. Section VI summarizes our work and provides an outlook for future study.

II. EXPERIMENTAL SETUP AND METHODS

Dy Rydberg-state spectroscopy is performed in a magneto-optical trap (MOT) operating on the broad transition ($\Gamma = 2\pi \times 32$ MHz, wavelength 421 nm) connecting the ground state to the $4f^{10}(^5I_8)6s6p(^1P_1^\circ)\,^5K_9$ excited state.

For technical reasons [35] and to maximize the number of trapped atoms, the MOT operates with two different detunings Δ: one for the vertical beams ($\Delta_V \simeq -3\Gamma/2\pi$) and another for the horizontal beams ($\Delta_H \simeq -\Gamma/2\pi$). Under these conditions, the trap contains approximately 10^4 atoms at a temperature of 60 mK. The MOT lifetime is about 5 ms, limited by population trapping in dark states [36].

Excitation to Rydberg states is achieved via a two-photon transition, as illustrated in Fig. 1(a). The first photon is directly provided by the MOT light, while a second probe laser [37] promotes atoms from the MOT excited state to highly excited Rydberg states. Under resonant conditions, this process introduces an additional loss channel for the MOT as a fraction of the trapped atoms are removed from the cooling cycle. As a result, Rydberg resonances manifest as a reduction of the MOT fluorescence, monitored with a photomultiplier tube while the probe laser is scanned. A similar technique has been used in the context of spectroscopy of Rydberg levels in Ho [38] and Sr [39]. We sketch in Fig. 1(b) the frequency range we explored, with a schematic representation of the Rydberg levels we expect to excite with our scheme, and in Fig. 1(c) the schematic of the magneto-optical trap.

The energy of each Rydberg state is determined measuring the wavelength of the two lasers with a 2-MHz-precision

wavemeter [40] whose absolute accuracy is kept on the same order by periodic calibration against a Sr atomic reference. This protocol guaranties an absolute uncertainty of 20 MHz over the whole explored energy range [41].

We report in Fig. 1(d) examples of experimental spectra obtained by scanning the probe-laser frequency at a rate of 5 GHz s^{-1}. Owing to the short MOT lifetime, this scan speed allows for a continuous measurement of the steady-state atom number. Each detected Rydberg level appears in the spectrum as a pair of twin depletion dips due to the bichromatic nature of the MOT light. This feature helps distinguishing Rydberg resonances from other single-dip signals, in general broader and less intense, probably originating from the absorption of two probe photons.

III. RESULTS AND DISCUSSION

In our survey, the probe laser has been scanned over a spectral range of approximately 250 cm^{-1} below the first ionization threshold $E_{\rm IP}$ (wavelength range between 414 and 419 nm, corresponding to the effective principal quantum numbers n ranging from 20 to 130), detecting more than 700 Rydberg levels [42]. Figure 2(a) shows the energy difference $\epsilon = E_n - E_{\rm IP}$ of all observed Rydberg levels with respect to the ionization threshold as a function of the assigned effective principal quantum number n^*. The latter is a noninteger quantity defined via the Rydberg-Ritz formula

$$E_n = E_{\rm IP} - \frac{R_{162}}{(n^*)^2} = E_{\rm IP} - \frac{R_{162}}{[n-\delta(n)]^2}, \qquad (1)$$

where $R_{162} = 109\,736.9439$ cm^{-1} is the reduced Rydberg constant for ^{162}Dy and $E_{\rm IP}$ denotes the first ionization threshold. From n^*, we compute the corresponding effective integer principal quantum number $n = \text{floor}(n^*) + 1$ as well as the noninteger part of the quantum defect $\delta(n) = \text{mod}[-n^*, 1]$ associated with a given Rydberg level. Using theoretical estimates [43] and the identified lowest-energy $4f^{10}6s7s$ and $4f^{10}6s6d$ states suggests that the integer part of the quantum defect is 4 for ns states and 2 for nd.

In Fig. 2(b) we report the noninteger part of the quantum defects of the measured levels, illustrating the evolution of δ with n. While the direct representation of Eq. (1) highlights the expected $1/n^2$ scaling of the binding energy relative to $E_{\rm IP}$, the energy dependence of quantum defects is particularly useful to resolve distinct Rydberg series, characterized by nearly constant values of δ, and to reveal the presence of perturbers. From our data we identify eight Rydberg series: two series with $0.32 \leqslant \delta \leqslant 0.45$ (theoretical estimates suggest these have ns character [43]); five series with $0.65 \leqslant \delta \leqslant 0.95$, consistent with theoretical estimates [43] for nd character; and a final nd series exhibiting a strong and broad perturbation. From the preceding paragraph, the full quantum defects are $4.32 \leqslant \delta \leqslant 4.45$ for ns and $2.65 \leqslant \delta \leqslant 2.95$ for nd.

The existence of eight Rydberg series can be anticipated through general angular momentum coupling arguments and selection rules. Since the intermediate state has total angular momentum $J = 9$, optical excitation allows access to Rydberg series with $J = 8, 9, 10$. Furthermore, the ionic core associated with the lowest-energy threshold of Dy^+ has character

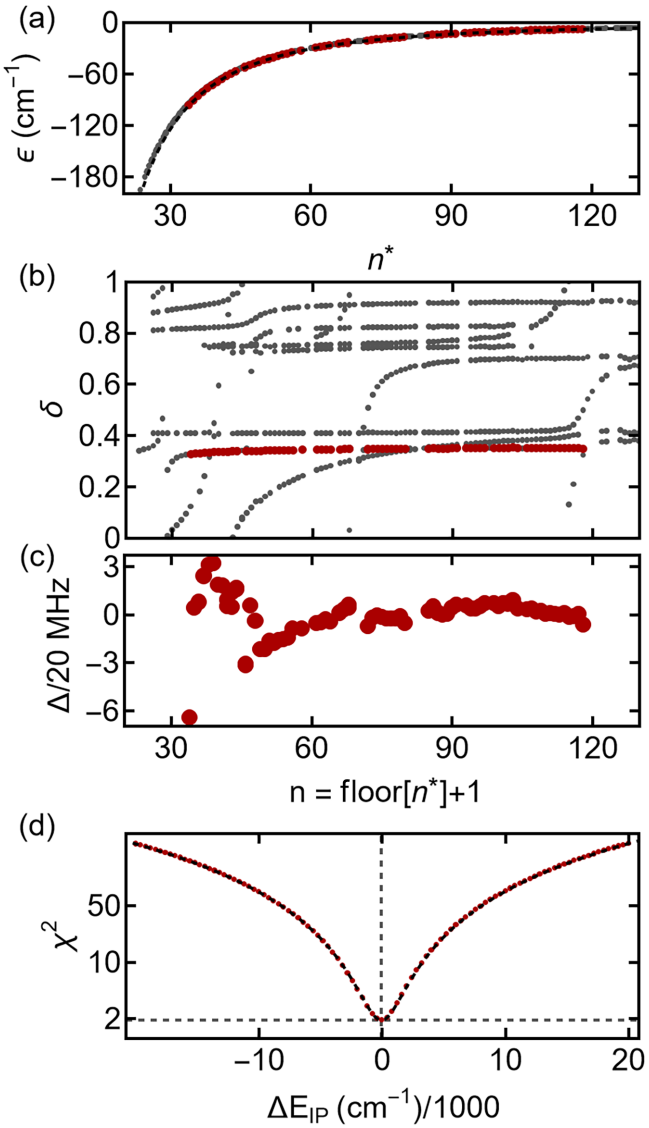

FIG. 2. (a) Measured energy difference $\epsilon = E_n - E_{\rm IP}$ of all observed Rydberg levels with respect to the ionization threshold $E_{\rm IP}$. (b) Plot of the corresponding quantum defects δ as a function of the effective integer quantum number n. Quantum defects are calculated from Eq. (1) using the estimated value of $E_{\rm IP}$. For both panels, gray points represent the full experimental dataset, while red points indicate the Rydberg levels used to extract the ionization potential $E_{\rm IP}$. The black dashed line in (a) is the best fit used to extract $E_{\rm IP}$. (c) Residuals Δ obtained from the best fit, expressed in units of the experimental uncertainty of 20 MHz (d) Dependence of the χ^2 value on $E_{\rm IP}$. The zero of the horizontal axis corresponds to 47 901.8265 cm^{-1}, which is our estimated value of $E_{\rm IP}$. The black dashed line shows a parabolic fit to the χ^2 dependence on $E_{\rm IP}$, used to determine the uncertainty in $E_{\rm IP}$. In (a) and (b) error bars are within the point size, while in (c) they are 1 by definition and thus they are not plotted.

$4f^{10}(^5I_8)6s(^2S_{1/2})\,^6I_{17/2}$. The ns Rydberg series converging to this threshold therefore have character $(17/2\ ns_{1/2})$ with total $J = 8$ or 9. The nd series converging to the same threshold can have either $(17/2\ nd_{3/2})$ or $(17/2\ nd_{5/2})$, both allowing $J = 8, 9, 10$ states. This leads to eight expected Rydberg

series (two *ns* and six *nd* orbital angular momenta, or three $J = 8$, three $J = 9$, and two $J = 10$ total angular momenta), in agreement with our observations and assuming the strongly perturbed series to belong to *nd*.

A. Determination of the ionization potential

We start our analysis by redetermining the ionization threshold E_{IP}. To extract it, we scan E_{IP} within a range roughly constrained by previous investigations [34].

For each tested value of E_{IP}, we compute $n = \mathrm{floor}(n^*) + 1$ and fit some of the observed energies of the *s* series with $J = 8$ (red points in Fig. 2 as well as Sec. III B for the character definition) using Eq. (1) together with the truncated expansion for the quantum defect,

$$\delta(n) = \delta_0 + \frac{\delta_2}{(n-\delta_0)^2} + \cdots . \tag{2}$$

These experimental points are chosen because they belong to the Rydberg series, among those observed, least affected by perturbers over a wide energy range at high n. Moreover, to reduce the effect of local electric fields, we intentionally excluded the highest-n data, which might be non-negligibly shifted. The overall range of n used to estimate the ionization potential is $33 \leqslant n \leqslant 118$, excluding $n = 46$ and 47 being affected by a sharp perturbation.

The optimal value of E_{IP} is obtained by minimizing the fit χ^2, as shown in Fig. 2(d), yielding a minimum value of $\chi^2 \simeq 1.9$. In Fig. 2(c) we report the best-fit residuals $\Delta = E_{\mathrm{meas}}(n) - E_{\mathrm{fit}}(n)$ in units of the experimental uncertainty (20 MHz).

Applying this procedure, we obtain

$$E_{\mathrm{IP}} = 47\,901.8265 \pm 0.0008\ \mathrm{cm}^{-1}, \tag{3}$$

which provides a new value of the first ionization limit with an uncertainty reduced by more than one order of magnitude but absolute value slightly outside the error bar of the last determination [34]. The uncertainty on E_{IP} is evaluated by fitting the computed $\chi^2(E_{\mathrm{IP}})$ with a parabola and extracting the 1σ confidence interval from the curvature, $\sigma = 1/\sqrt{d\chi^2/dE_{\mathrm{IP}}^2}$. As a cross-check, this fitting procedure is also applied to $J = 9$ *ns* and $J = 10$ *nd* data, producing consistent thresholds but with a substantially larger χ^2 value.

From the same fit we obtain $\delta_0 = 0.3514(2)$ and $\delta_2 = -27.4(3)$. While δ_0 is in approximate agreement with the value obtained from the MQDT analysis of Sec. IV A, the extracted δ_2 substantially differs from the MQDT result. This discrepancy is expected because Eq. (2) does not explicitly account for the energy dependence induced by perturbing levels from other Rydberg series. In particular, in this case a perturber located at 143 cm^{-1} below the first ionization threshold (see Sec. IV A) contributes to the apparent energy dependence of $\delta(n)$ and therefore affects the fitted value of δ_2.

B. Patterns from angular momentum constraints

Although the presence of perturbers complicates the spectrum shown in Fig. 2(b), these perturbations can be exploited to group and assign the observed Rydberg series. In particular, due to the independence of distinct total angular momentum J manifolds, if a single perturber affects two series, then the two series must belong to the same J manifold. Moreover, the perturbation strength is enhanced when the perturber shares the same orbital character. For instance, an *ns* perturber predominantly affects an *ns* Rydberg series, while its influence on *nd* series is typically weaker.

The first excited state of Dy^+ has character $4f^{10}(^5I_8)6s(^2S_{1/2})\,^6I_{15/2}$ and lies 828.314 cm^{-1} above the ionic ground state $4f^{10}(^5I_8)6s(^2S_{1/2})\,^6I_{17/2}$ [44]. Rydberg states converging to this excited threshold can therefore act as perturbers for series attached to the lower threshold. Given our explored energy range, approximately 250 cm^{-1}, we expect only a small number of such perturbers, corresponding to effective principal quantum numbers in the approximate range $n^*_{15/2} \simeq 10$–11.5.

To identify these perturbers, we use the energy relative to the ionization potential, $\epsilon = E - E_{\mathrm{IP}}$, to define the quantity

$$\delta_{15/2}(\epsilon) = \mathrm{mod}\left(-\sqrt{\frac{R_{162}}{828.314 - \epsilon}}, 1\right), \tag{4}$$

which estimates the quantum defect a perturber converging to the Dy^+, $J = 15/2$ threshold would have as a function of its energy detuning ϵ from the first ionization threshold E_{IP}. This estimate is shown as black lines in Fig. 3.

Because the first-excited ionic core has $J = 15/2$, the corresponding *ns* series can only have total angular momentum $J = 7$ or $J = 8$. Therefore, the observation of a perturber predominantly affecting an *ns* series strongly suggests that the perturbed series belongs to the $J = 8$ manifold. This is precisely the situation for the perturbation located at $\epsilon \simeq -143\ \mathrm{cm}^{-1}$, highlighted by the red shaded region in Fig. 3. In this region $\delta_{15/2} \simeq 0.38$, consistent with an *ns* perturber, supporting an interpretation in terms of coupling to an *ns* series converging to the Dy^+ excited threshold. This argument unambiguously assigns the series with unperturbed quantum defect $\delta \simeq 0.35$ to the $J = 8$ manifold.

The identification of the remaining $J = 8$ series can be completed by noting that the two Rydberg series with unperturbed quantum defects $\delta \simeq 0.90$ and $\delta \simeq 0.82$ share a common perturbation at $\epsilon \simeq -52\,\mathrm{cm}^{-1}$ with the above-described $J = 8$ *ns* series. For this second perturber, $\delta_{15/2} \simeq 0.84$, suggesting an *nd* character. This also explains the stronger perturbation observed on the two *nd* series compared to the *ns* series. Beyond identifying the $J = 8$ manifold, the reasonable values of $\delta_{15/2}$ suggest that both perturbers belong to Rydberg series converging to the first excited Dy^+ threshold.

Again using the fact that a perturber can only perturb series with the same J, we note from Fig. 3 that the perturber located at $\epsilon \simeq -8\,\mathrm{cm}^{-1}$ affects three different series. This implies that these three series form the $J = 9$ manifold because, as noted above, there are three $J = 9$ series and two $J = 10$ series. Among them, the series with unperturbed quantum defect $\delta \simeq 0.41$ is assigned to *ns* character, while the other two are *nd* series, including the one exhibiting a broad perturbation centered around $\epsilon \simeq -70\ \mathrm{cm}^{-1}$.

Finally, by elimination, the two remaining series should have *nd* character and should have $J = 10$. This is confirmed

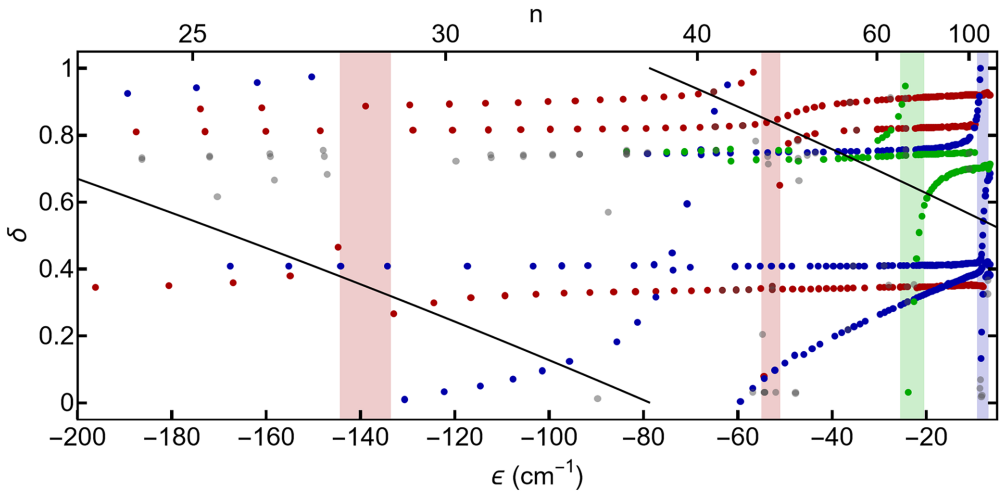

FIG. 3. Quantum defects of assigned Rydberg levels, divided in series for different values of J. Red points correspond to $J = 8$, blue to $J = 9$, and green to $J = 10$. The colored shaded areas indicate the position of the perturbers used for series grouping (see the text for details). The black line represents the quantum defect $\delta_{15/2}$ calculated from Eq. (1) using the first excited ionization threshold; the discontinuity occurs when $n^*_{15/2}$ becomes equal to 11.

since they share a common perturber, the perturber at $\epsilon \simeq -22$ cm^{-1}, showing they have the same J. Also, both of their unperturbed quantum defects $\delta \simeq 0.73$ are consistent with the expected values for nd character.

While the analysis based on constraints imposed by angular momentum was able to assign many of the observed levels, for others this approach is too simplistic. This is the case, for instance, for the points with n between 35 and 90 and $\delta \simeq 0.72$, where many different lines have similar quantum defects. To refine the assignment and to study the effect of the observed perturbers more quantitatively, in the next section we fit our data with a simplified parametrization of MQDT.

IV. MQDT APPROACH

In this section we describe how we use ideas from MQDT [45] to understand some properties of the observed Rydberg states. In particular, we show how perturbers affect the series MQDT parameters, giving a quantitative description of the observed levels at near experimental uncertainty. We fit the line positions over a range of approximately 250 cm^{-1} (approximately 7.5 THz) with standard deviations of approximately 150, 110, and 70 MHz for the $J = 8$, 9, and 10 series, respectively. The goal is to use the MQDT fit to classify lines within each series and to identify Rydberg states that are strongly modified by perturbing states attached to higher thresholds. Moreover, we use ideas from the frame transformation approximation to understand the energy of the $J = 8$ ns perturber.

We use the representation where a real, symmetric K matrix gives the coupling between the different channels, i.e., between the different Rydberg series. The equations of MQDT for a single threshold, as we are modeling for Dy, show that the bound states are determined by

$$\det[\mathbf{K}(\epsilon) + \tan \pi \nu(\epsilon)\mathbf{I}] = 0, \tag{5}$$

where $\epsilon = E - E_{\rm IP}$ is the energy in cm^{-1} relative to the threshold, $\mathbf{I}$ is the unit matrix, and $\nu(\epsilon) = \sqrt{-R_{162}/\epsilon}$. Note that (i) $\nu(\epsilon)$ is defined for any negative energy value ϵ, while n^*, which shares the same definition, has value only for the actual bound states, and (ii) any unitary transformation of the K matrix, $\tilde{\mathbf{K}} = \mathbf{U}\mathbf{K}\mathbf{U}^\dagger$ with $\mathbf{U}$ a unitary matrix, will still satisfy Eq. (5), so a fit of $\mathbf{K}$ typically constrains only the eigenvalues.

When the perturbers are separated in energy, the K matrix can be approximated by the form

$$K_{ij}(\epsilon) = \delta_{ij} \tan \pi \delta_i(\epsilon) - \frac{V_{i,1}V_{j,1}}{\epsilon - E_1} - \frac{V_{i,2}V_{j,2}}{\epsilon - E_2} - \cdots, \tag{6}$$

where the quantum defects $\delta_i(\epsilon)$ slowly depend on energy, E_α is the energy of the αth perturber, and the $V_{i,\alpha}$ are real numbers that parametrize the interaction of the αth perturber with channel i. Given the fact that series with different angular momentum J do not interact in the absence of external fields, channels with different J are treated separately. For one channel and one perturber, the energy width of the interaction is $\Gamma = 2V^2/(1 + \tan^2 \pi\delta)$. For more channels, the relations are more complicated, but, roughly, larger $|V_{i,\alpha}|$ means perturber α has a larger effect on channel i. A sketch of the derivation of this form is given in Appendix B. Because the fit does not constrain a unitary transformation of $\mathbf{K}$, we have chosen to have the slowly varying portion of Eq. (6) be diagonal. The $\delta_i(\epsilon)$ can have the form of Eq. (2) or an equivalent, easier to implement form

$$\delta_i(\epsilon) = \delta_{0,i} + \epsilon \left.\frac{d\delta_i(\epsilon)}{d\epsilon}\right|_{\epsilon=0}, \tag{7}$$

where the $\delta_{0,i}$ and the derivative are evaluated at threshold. This form is related to that in Eq. (2) through $\delta_{2,i} = -R_{162} d\delta_i(\epsilon)/d\epsilon$. The difference between the two forms is δ_2^2/ν^5, which is negligible for our states and accuracy.

The results of the fitting are shown in Fig. 4, where the lines are obtained by taking the arctangent of the eigenvalues of the energy-dependent K matrix at each energy then dividing by π; we use the definition of arctangent so the result is between 0 and 1. When the energy exactly equals one of the perturber's energies $\epsilon = E_\alpha$, one of the eigenquantum defects equals 1/2.

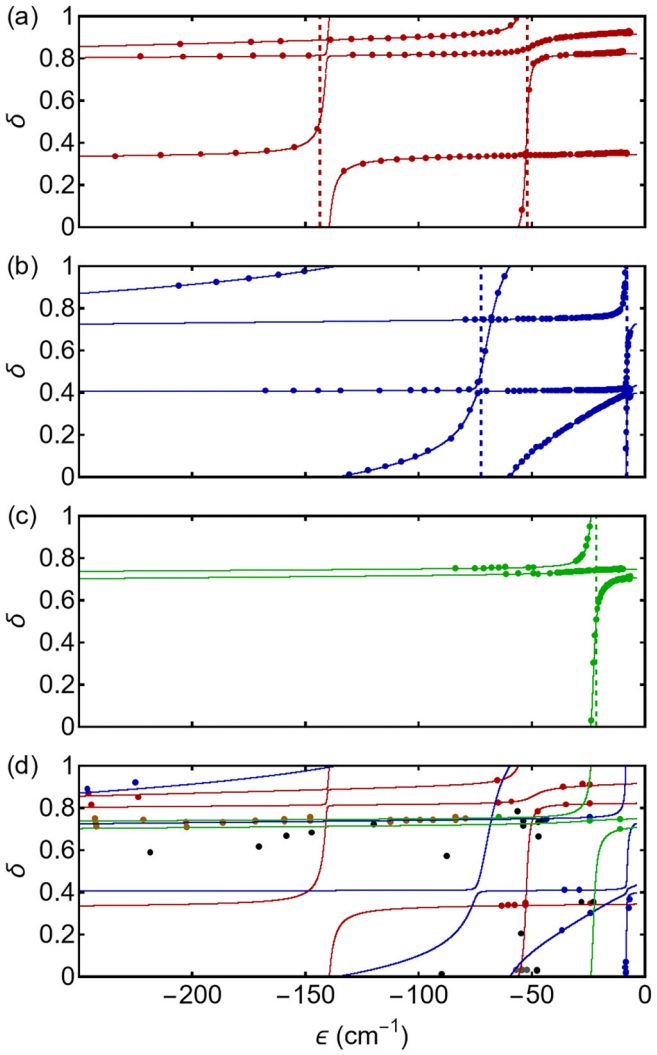

FIG. 4. Results of MQDT calculations compared with the experimental data for the Rydberg series with (a) $J = 8$, (b) $J = 9$, and (c) $J = 10$. The fitting routine is also used to assign a total angular momentum J to each experimental data point. The vertical dashed lines represent the position of the perturbers reported in Table II. The $J = 9$ case possesses a perturber not shown in the figure, located above E_{IP}. (d) Experimental data points that remain unassigned. Red and blue points indicate points suspected to correspond to $J = 8$ and 9, respectively, because they are quite near a quantum defect line from the fit, but a physical constraint disqualifies it for that J. Orange points represent experimental data having either $J = 9$ or $J = 10$. Gray points may belong to a Rydberg g series, as suggested by their small quantum defect. Black points are not assigned either because theoretical predictions for different series are nearly indistinguishable or because the experimental values deviate too strongly from the theoretical expectations. Data from the MQDT fit are available from [46].

A. Results of MQDT fit

We fixed the threshold to the value in Eq. (3), allowed all parameters defining the K matrix (6) to vary, and fit these parameters by minimizing the reduced χ^2. The number of fit parameters is

$$N_{\mathrm{fit}} = 2N_{\mathrm{ch}} + N_{\mathrm{pert}} \times (N_{\mathrm{ch}} + 1), \tag{8}$$

TABLE I. MQDT fit with Eqs. (2) and (7). Fits for the quantum defects δ_0 and δ_2 are provided for the eight observed series. The number in parentheses is the parameter width from the fit. See Appendix A for a discussion of the uncertainty in the MQDT fit parameters.

J	$\delta_{0,i}$	$\delta_{2,i}$
8	0.34710(17)	–7.73(12)
8	0.82402(23)	–9.65(19)
8	0.92174(24)	–29.87(19)
9	0.40740(26)	–0.09(21)
9	0.88622(20)	–37.48(15)
9	0.74936(65)	–11.42(1.2)
10	0.72236(66)	–9.4(1.7)
10	0.75275(48)	–7.43 (80)

where N_{ch} is the number of channels and N_{pert} is the number of perturbers for that J. The first term in N_{fit} is from Eq. (7) and the last term is from the perturbers. We use these parameters for the series to fit 245 ($J = 8$), 256 ($J = 9$), and 119 ($J = 10$) energies using 14 ($J = 8$), 18 ($J = 9$), and 7 ($J = 10$) parameters. The minimum values for the χ^2 are 57.2, 29.2, and 11.8 for $J = 8$, 9, and 10 respectively. These large values of χ^2 are due to an oversimplified modeling, with a reduced number of perturbers and couplings [47].

The $\delta_{0,i}$ and $\delta_{2,i}$ for each of the eight Rydberg series identified are reported in Table I. As a point of comparison, the τ_0, τ_2 in Table II of Ref. [33] (corresponding to our δ_0, δ_2) are 0.301, −15.78 and 0.427, −1.718 for the ns series in Er compared with 0.347, −7.7 and 0.407, ~ 0 for our fits to the Dy ns series. The values are not expected to be the same since the specific values depends on details of angular momentum coupling, but they should be similar.

In Table II we report the values for all the perturbers identified from the MQDT fit. Each perturber is also associated with two or three coupling coefficients $V_{i,\alpha}$, depending on the value of J of the perturbing state. The discussion of the uncertainty in the fitting parameters is in Appendix A.

From the MQDT fits we obtained precise estimates of the perturber energies, which can be used to gain insight into their physical nature.

TABLE II. MQDT fit with Eq. (6) for perturber parameters. The number in parentheses is the parameter width from the fit. See Appendix A for a discussion of the uncertainty in the MQDT fit parameters. The perturber at −143.70 cm^{-1} in the ns series has already been reported in Ref. [34], and the strongly perturbed series corresponding to the level at 9.95 cm^{-1} has been observed but not interpreted.

J	E_α (cm^{-1})	$V_{1,\alpha}$ (cm$^{-1/2}$)	$V_{2,\alpha}$ (cm$^{-1/2}$)	$V_{3,\alpha}$ (cm$^{-1/2}$)
8	–52.051(16)	0.002(43)	0.641(13)	1.0016(74)
8	–143.696(30)	2.7674(86)	0.146(69)	0.057(85)
9	9.95(14)	1.22(13)	8.0639(64)	1.208(63)
9	–7.939(39)	0.606(93)	–0.14(18)	0.818(27)
9	–72.453(26)	0.670(40)	2.5305(52)	0.150(20)
10	–21.5292(94)	1.3547(57)	0.9425(65)	

As already discussed in Sec. III B, most of the observed perturbers can be confidently identified as Rydberg levels attached to the first excited state of Dy^+. In particular, for the perturbers affecting the $J = 8$ manifold at -143.696 and $-52.050\ \mathrm{cm}^{-1}$, the $J = 10$ perturber observed at $-21.527\ \mathrm{cm}^{-1}$, and two of the $J = 9$ perturbers with negative energies at -72.451 and $-7.932\ \mathrm{cm}^{-1}$, we can evaluate the effective quantum number $n^*_{15/2}$ and the corresponding quantum defect $\delta_{15/2}$ as defined in Sec. III B. This yields the pairs (10.625, 0.375), (11.165, 0.835), (11.363, 0.637), (11.037, 0.963), and (11.455, 0.545), respectively.

All of these values correspond to plausible quantum defects for *ns* (the first case) and *nd* (the remaining cases) Rydberg series. The only apparently anomalous value is the quantum defect obtained for the $J = 9$ perturber at $-7.932\ \mathrm{cm}^{-1}$. However, the value $\delta_{15/2} = 0.545$ might be explained by using guidance from the channel-dependent defects δ_i extracted from our fits. We find that values within the range of this table could lead to this quantum defect. For instance, taking δ_0 to be a small *nd* value from Table I (e.g., $\delta_0 = 0.72$) and δ_2 to have a moderate magnitude (e.g., $\delta_2 = -20$), one obtains a total quantum defect $\delta_{15/2} = 0.72 - \frac{20}{11.28^2} \approx 0.56$, which is consistent with the fitted value. This suggests the interpretation of this perturber as having predominantly 15/2 *nd* character.

The final perturber to consider is the positive-energy $J = 9$ state observed at $9.95\ \mathrm{cm}^{-1}$. Applying the same procedure yields $(n^*_{15/2}, \delta_{15/2}) = (11.581, 0.419)$, which would nominally suggest an *ns* character. However, the $J = 9$ manifold with 15/2 character does not support an *s* series since $(15/2\ ns_{1/2})$ can only give $J = 7$ and 8. The exceptionally strong coupling of this level to the other fitted Rydberg series instead leads us to tentatively interpret this perturber as an $nd_{3/2}$ or $nd_{5/2}$ Rydberg level attached to the second excited ionic state $4f^{10}(^5I_7)6s(^2S_{1/2})\ ^6I_{15/2}$, which lies $4341.104\ \mathrm{cm}^{-1}$ above the first ionization threshold. Under this assignment, the corresponding quantum defect is $\delta \approx 0.966$, which is nearer the range of *nd* quantum defects in Table I and could have $J = 9$. This would give an effective quantum number $n^* \approx 5.034$. The small value of n^* would imply that the perturber is strongly bound, which could also explain the large coupling strength observed.

Finally, we stress that MQDT fits have also been used to spot the rare misidentifications (much less than 1% of the total) within the experimental data, which mainly originated from mode jumps or instabilities of the probe laser.

B. Frame transformation for *ns*

For many atoms with *ns* and *nd* Rydberg states, perturbers interact most strongly with series with the same outer angular momentum. Thus, *ns* series tend to weakly interact with *nd* perturbers attached to higher thresholds and *nd* series tend to weakly interact with *ns* perturbers. As discussed in the preceding section, this suggests that the perturber at $-143.696\ \mathrm{cm}^{-1}$ has *ns* character attached to the 15/2 threshold. This was the main clue for distinguishing the $J = 8$ and 9 series since only $J = 8$ has *ns* Rydberg series attached to the 15/2 threshold.

To make this assignment more firm, we use ideas from the frame transformation approximation (Sec. II E of Ref. [45]) for the two *ns* series and the *ns* perturber. The basic idea behind the frame transformation is that *LS* coupling is a good approximation when the Rydberg electron is at small distances. This gives a phase shift that depends on whether the 6*s* and *ns* electrons are coupled to singlet or triplet, but it does not couple the two even though they have the same total *J* after coupling with the $4f$ electrons. However, when the Rydberg electron is more than approximately $20a_0$ beyond the core electrons, it is more appropriate for the 6*s* electrons to be coupled to the $4f$ electrons to give a *J* for the core and then the Rydberg electron's angular momentum is coupled to the core angular momentum. These two regions can be connected through a unitary transformation which arises from the different order of angular momentum coupling. The main point is that this approximation gives four *K*-matrix elements in terms of two phase shifts. If the data from the two *ns* series and one *ns* perturber can be represented this way, that gives a strong indication that the identifications of the *J* for the different series are correct.

TABLE III. Comparison between the MQDT fitting and frame transformation (FT) approximation for the two *ns* Rydberg series.

K-matrix parameter	MQDT fit	FT approximation
$K^{(9)}_{17/2,17/2}$	3.340	3.259
$K^{(8)}_{17/2,17/2}$	1.918	2.145
$K^{(8)}_{15/2,15/2}$	2.414	2.268
$K^{(8)}_{15/2,17/2}$	0.947	1.051

Appendix C gives the details of the frame transformation which leads to four *K*-matrix parameters given in terms of a specified frame transformation matrix and two unspecified diagonal elements [Eq. (C4)]. From Eq. (B3) with $E_{15/2} - E_\alpha = 972.01\ \mathrm{cm}^{-1}$ and $\nu_\alpha = 10.625$, we calculate all four matrix elements from experimental data,

$$\begin{aligned} K^{(9)}_{17/2,17/2} &= \tan(0.4074\pi) = 3.340, \\ K^{(8)}_{17/2,17/2} &= \tan(0.3470\pi) = 1.918, \\ K^{(8)}_{15/2,15/2} &= \tan(0.375\pi) = 2.414, \\ K^{(8)}_{15/2,17/2} &= V\sqrt{\frac{d\tan\pi\nu}{d\epsilon}} = 0.947, \end{aligned} \tag{9}$$

where we used $V = 2.767\ \mathrm{cm}^{-1/2}$. We used these four values and the form (C4) in χ^2 to find the best values for the two unknowns. The χ^2 minimization gave $K_{^3S} = 3.259 = \tan(0.405\pi)$ and $K_{^1S} = 1.154 = \tan(0.273\pi)$. By using these values in Eq. (C4), we can compare MQDT fitting and the frame transformation approximation. Results are shown in Table III, where the rightmost values are from Eq. (C4).

This is reasonable agreement for such a simple approximation. Recall that we are using the same quantum defect whether it is relative to the 17/2 or 15/2 threshold, while the fits to the Rydberg series attached to the 17/2 thresholds suggest the values for δ_2 are not 0. The largest difference in the diagonal elements is for $K^{(8)}_{17/2,17/2}$ and corresponds to a difference in quantum defect of 0.014.

A similar transformation could be performed for the *nd* series. However, we did not attempt this study since these

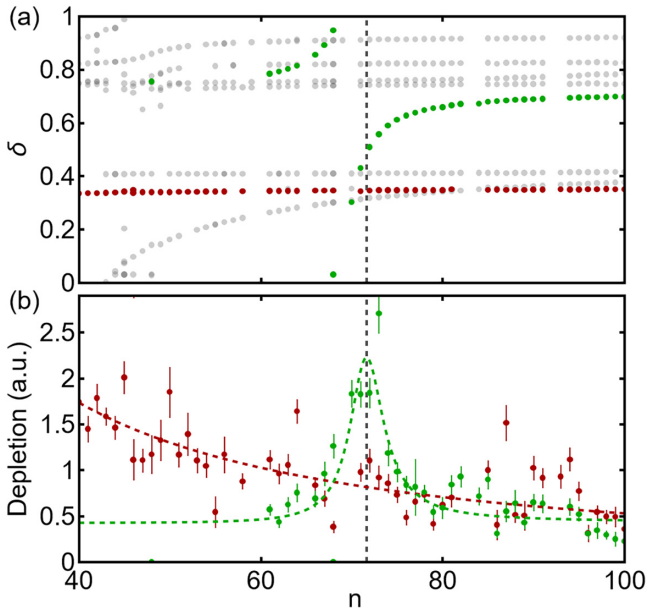

FIG. 5. (a) Quantum defects of all eight observed Rydberg series as a function of n. Shown in red is the unperturbed $J = 8$ and in green the perturbed $J = 10$ Rydberg series reported in (b). (b) Amplitude of the depletion signals for the two $J = 8$ and $J = 10$ Rydberg series. Dashed lines are best-fit functions (see the text for details).

transformations will lead to 4×4 matrices and our fit data do not give all of the relevant parameters.

V. INTENSITY OF DEPLETION LINES

Most applications of Rydberg states, either implying resonant Rabi flopping or off-resonance dressing, require a thorough characterization of the spectrum, integrating the tabulation of the resonance frequencies with additional information on the oscillator strength and lifetime of the excited state. In this respect, since our spectroscopic investigation is performed at fixed laser intensity, applying a naive approach, one might expect to extract the oscillator strength from the amplitude of the depletion signal. We find that, at least in the clearest case of $J = 10$, such an analysis is able to reveal the peaked modulation in the presence of a pertuber, originating from the coupling with a state of lower principal quantum number. Figure 5 shows the experimental measurements of the depletion signal (defined as the product of the signal amplitude and its full width at half maximum) associated with the strongly perturbed $J = 10$ series and the least perturbed ns $J = 8$ series (the one selected for the estimation of E_{IP}). In the former case, the trend exhibits a pronounced resonance around $n \simeq 72$, whereas in the latter it decreases monotonically with increasing principal quantum number. By assuming a Lorentzian behavior with coupling Γ in the energy domain, we fit the experimental data obtained in the presence of a perturber using the phenomenological function

$$f(n^*) = \alpha \frac{1}{1 + [\epsilon(n^*) - \epsilon_0]^2 / (\Gamma/2)^2}, \tag{10}$$

where α is the amplitude of the feature in the depletion signal; Γ denote the coupling strength between the Rydberg series and the perturber; and $\epsilon(n^*)$ and ϵ_0 represent the detuning as determined by Eq. (1) and the energy position of the perturber, respectively, both relative to the first ionization limit. From the fit, we extract a resonance position at -21.4 ± 0.2 cm^{-1} and a coupling strength $\Gamma = 2.8 \pm 0.6$ cm^{-1}. While the position of the perturber is in agreement with the MQDT calculations reported in Table II, its width is only compatible. Conversely, for the unperturbed series, the data are fitted with a power-law dependence $n^{-\beta}$, yielding $\beta = 1.3 \pm 0.3$. Although this behavior clearly indicates a monotonic decrease of the depletion signal with increasing n, the fit results show that the oscillator strength alone is insufficient to fully describe the observed trends, as it would determine a $1/n^3$ dependence.

In fact, the dependence of the MOT loss rate on the Rydberg excitation is determined by the combination of a number of processes with different trends over n [48]. Moreover, the interpretation of the signal is further complicated as we probe the absolute population in the intermediate state of a three-level ladder system with incoherent constant inflow and variable losses. For these reasons, we do not expect the depletion signal to provide a direct or quantitative measure of the oscillator strength.

Despite these limitations, the depletion observable allows us to clearly distinguish qualitative differences induced by the presence of a perturber. Remarkably, a quantitative analysis of the $J = 10$ series yields results consistent with MQDT predictions, thereby providing an independent benchmark of the theoretical model. A more comprehensive comparison between the experimental spectra (including the other lines) and the oscillator strengths evaluated within MQDT would require a detailed and quantitative characterization of all the physical mechanisms responsible for the depletion, which goes beyond the scope of the present work.

VI. CONCLUSION AND OUTLOOK

We have presented the first high-resolution Rydberg spectroscopy of ^{162}Dy, realized by observing trap depletion in a magneto-optical trap. We classified more than 600 levels (over roughly 700 detected ones), assigning them to the eight expected Rydberg series we can explore with our excitation scheme. Additionally, our measurements yield an improved estimate of the first ionization energy, refined by an order of magnitude compared to previous studies. The experimental data are supported by MQDT fits. Besides confirming and completing the identification of the Rydberg series, MQDT fits have been used to estimate the position and the coupling of the six observed perturbers within the explored energy region. Finally, by analyzing the amplitude of the depletion signal, we qualitatively observed how a perturber enhances the coupling to the Rydberg series it is affecting.

From a spectroscopic standpoint, a natural extension of this work would be to conduct high-resolution spectroscopy in the presence of magnetic [33] or electric fields, in order to further validate the line assignments presented here. This would also allow for the precise determination of the polarizability of the Rydberg states.

Although our present study deals with the excitation of low-n Rydberg states from the external $6s$ shell, many intriguing possibilities may arise from the simultaneous

excitation of an internal isolated-core $4f$ electron. Fast autoionization of these states could be mitigated as in the Yb case [49], giving access to optical trapping of Rydberg atoms, eventually with high-l excitation [50], and double-Rydberg studies [51].

ACKNOWLEDGMENTS

We acknowledge support from the European Union through the ERC SUPERSOLIDS Project No.101055319, and the QuantERA Programme, project MAQS, under Grant Agreement No. 731473, with funding organization Consiglio Nazionale delle Ricerche. We acnowledge support from the National Quantum Science and Technology Institute (NQSTI), funded by the European Union NextGenerationEU, NRRP (National Recovery and Resilience Plan) Mission 4, Component 2, Investment 1.3 - Project PE00000023, CUP B53C22004180005. A.F. and L.T. acknowledge funding from the Italian MUR (PRIN DiQut Grant No. 2022523NA7). F.R. was supported by the National Science Foundation under Award No. 2410890-PHY. We thank Giulia Semeghini, Igor Ferrier-Barbut, Antoine Browaeys, Steven Lepoutre, Patrick Cheinet, Daniel Comparat, and Thomas Gallagher for very fruitful discussions. We thank Leonardo Salvi and his team for providing the high-resolution wavemeter and its calibration.

DATA AVAILABILITY

Data from the MQDT fit used in Fig. 4 are available from [46]. Raw spectroscopic data are available in [42].

APPENDIX A: UNCERTAINTY IN MQDT FIT PARAMETERS

To obtain an estimate of the uncertainty in the fit parameters, we do not use the full variance matrix. We vary one parameter at a time. For a given parameter Q, one-half the separation of the two values that give $\chi^2_{\min}+1/2$ defines ΔQ. For $J=10$, there is only one perturber, so the signs of V cannot be found from the fitting procedure. For the other J, we found that we could change the sign of the $V_{i,\alpha}$ and get nearly as good fits but with some other parameters changing in size, some of them beyond the listed values of their width. As an example, changing the 0.641 $\mathrm{cm}^{-1/2}$ for the $J=8$ resonance at -52.051 cm^{-1} to a negative value left the χ^2 almost unchanged and hardly changed any of the other parameters; clearly, the uncertainty in this parameter is not the 0.013 $\mathrm{cm}^{-1/2}$ listed in the table since either value is acceptable. As another example for $J=9$, when we set the $V_{1,\alpha}=1.22$ $\mathrm{cm}^{-1/2}$ for the 9.95-cm^{-1} perturber to be negative, the minimization gave the other coupling parameters outside the range from the original χ^2 fit by factors less than 2.

APPENDIX B: DERIVATION OF THE K MATRIX NEAR PERTURBERS

In this appendix we give a brief derivation of the approximation of Eq. (6). To simplify the derivation, we will only consider two thresholds. The higher-energy threshold leads to perturbers for the lower thresholds. In the sense of MQDT, the K matrix including both thresholds hardly has an energy dependence. Channels attached to the lower threshold will get subscript r (for Rydberg) and those attached to the upper threshold will get subscript p (for perturber). We can perform a unitary transformation on the K matrix so that the part of the K matrix in the perturber space and the part in the Rydberg space are each diagonal. Applying the bound-state boundary conditions to the perturber channels [45] gives the K matrix

$$K_{r,r'}=\delta_{r,r'}\tan\pi\delta_r-\sum_p\frac{K_{r,p}K_{p,r'}}{\tan\pi\nu_p+\tan\pi\delta_p}, \tag{B1}$$

where the $K_{r,r'}$ is the K matrix in the Rydberg space after applying the boundary conditions to the perturbers, $\tan\pi\delta_r$ and $\tan\pi\delta_p$ are the diagonal elements of the K matrix in the Rydberg and perturber space, respectively, before applying the boundary conditions, and $\nu_p=\sqrt{R_{162}/(E_p-E)}$, with E_p the energy of the perturber threshold. This form does not have an approximation.

When the perturber threshold leads to $\nu_p\ll\nu_r$ as is the case for Dy, the Eq. (B1) can be approximated for energies where $\tan\pi\nu_p\sim-\tan\pi\delta_p$. For each of the channels p near their resonance, we approximate in the neighborhood of the resonance

$$\tan\pi\nu_p=-\tan\pi\delta_p+(\epsilon-E_\alpha)\left.\frac{d\tan\pi\nu}{d\epsilon}\right|_{\epsilon=E_\alpha} \tag{B2}$$

to first order in $\epsilon-E_\alpha$. Trigonometric identities can be used to evaluate the derivative

$$\left.\frac{d\tan\pi\nu}{d\epsilon}\right|_{\epsilon=E_\alpha}=\frac{\pi}{2}\frac{\nu_\alpha}{E_p-E_\alpha}(1+\tan^2\pi\nu_\alpha), \tag{B3}$$

where E_p is the threshold energy for the excited core state and E_α is relative to the ground core energy.

Using this approximation for the energy dependence, the exact Eq. (B1) can be approximated as Eq. (6) with the identification

$$V_{i,\alpha}=K_{r_i,p_\alpha}\Big/\sqrt{\left.\frac{d\tan\pi\nu}{d\epsilon}\right|_{\epsilon=E_\alpha}}. \tag{B4}$$

APPENDIX C: DETAILS OF FRAME TRANSFORMATION

If there is an angular momentum coupling at small distances, β, that approximately commutes with the Hamiltonian but coupling b is more appropriate when the electron is far from the core, then the K matrix in the b representation is

$$K_{b,b'}=\sum_\beta U_{b,\beta}K_\beta U^\dagger_{\beta,b'}, \tag{C1}$$

where $U_{b,\beta}=\langle b|\beta\rangle$.

For the ns series described in Sec. IV B, the transformation matrix is determined by the recoupling of angular momentum. The β-type coupling gives the three kets with the form $|[j_1(j_2,j_3)J_{23}]J\rangle$, where j_1 is the total angular momentum of the $4f$ electrons, j_2 and j_3 are the spins of the $6s$ and ns electrons, and J_{23} is the total spin coupling of the $6s$ and ns electrons: $|[8(1/2,1/2)0]8\rangle$, $|[8(1/2,1/2)1]8\rangle$, and $|[8(1/2,1/2)1]9\rangle$ since the orbital angular momentum from the $6s$ and ns electrons is 0 for all

couplings. The b-type coupling gives three kets with the form $|[(j_1, j_2)J_{12}j_3]J\rangle$, where the j_1, j_2, and j_3 are as before and J_{12} is the total angular momentum of the core electrons ($4f$ and $6s$): $|[(8, 1/2)15/2, 1/2]8\rangle$, $|[(8, 1/2)17/2, 1/2]8\rangle$, and $|[(8, 1/2)17/2, 1/2]9\rangle$. The $J = 9$ only has one state in each coupling and therefore $U = 1$. For $J = 8$, the U is a 2×2 matrix given by the projections $\langle b|\beta\rangle$ and is proportional to a $6j$ coefficient,

$$U_{a,\alpha} = \langle[(j_1, j_2)J_{12}j_3]J|[j_1(j_2, j_3)J_{23}]J\rangle = (-1)^{j_1+j_2+j_3+J}[J_{12}, J_{23}]\begin{Bmatrix} j_1 & j_2 & J_{12} \\ j_3 & J & J_{23} \end{Bmatrix}, \quad \text{(C2)}$$

where $[J_{12}, J_{23}] \equiv \sqrt{(2J_{12}+1)(2J_{23}+1)}$. If the $\beta = 1, 2$ coupling are $J_{23} = 0, 1$ and the $b = 1, 2$ coupling are $J_{12} = 17/2, 15/2$, then

$$U = \begin{pmatrix} \sqrt{\frac{9}{17}} & \sqrt{\frac{8}{17}} \\ -\sqrt{\frac{8}{17}} & \sqrt{\frac{9}{17}} \end{pmatrix}. \quad \text{(C3)}$$

Using this transformation matrix, the four K-matrix elements for the ns series are

$$\begin{aligned} K^{(9)}_{17/2,17/2} &= K_{^3S}, \\ K^{(8)}_{17/2,17/2} &= \tfrac{9}{17}K_{^1S} + \tfrac{8}{17}K_{^3S}, \\ K^{(8)}_{15/2,15/2} &= \tfrac{8}{17}K_{^1S} + \tfrac{9}{17}K_{^3S}, \\ K^{(8)}_{15/2,17/2} &= -\frac{\sqrt{72}}{17}K_{^1S} + \frac{\sqrt{72}}{17}K_{^3S}. \end{aligned} \quad \text{(C4)}$$

[1] C. S. Adams, J. D. Pritchard, and J. P. Shaffer, Rydberg atom quantum technologies, J. Phys. B **53**, 012002 (2019).

[2] M. Saffman, T. G. Walker, and K. Mølmer, Quantum information with Rydberg atoms, Rev. Mod. Phys. **82**, 2313 (2010).

[3] A. Browaeys and T. Lahaye, Many-body physics with individually controlled Rydberg atoms, Nat. Phys. **16**, 132 (2020).

[4] M. A. Norcia, A. W. Young, W. J. Eckner, E. Oelker, J. Ye, and A. M. Kaufman, Seconds-scale coherence on an optical clock transition in a tweezer array, Science **366**, 93 (2019).

[5] I. S. Madjarov, A. Cooper, A. L. Shaw, J. P. Covey, V. Schkolnik, T. H. Yoon, J. R. Williams, and M. Endres, An atomic-array optical clock with single-atom readout, Phys. Rev. X **9**, 041052 (2019).

[6] O. Firstenberg, C. S. Adams, and S. Hofferberth, Nonlinear quantum optics mediated by Rydberg interactions, J. Phys. B **49**, 152003 (2016).

[7] J. Kumlin, C. Braun, C. Tresp, N. Stiesdal, S. Hofferberth, and A. Paris-Mandoki, Quantum optics with Rydberg superatoms, J. Phys. Commun. **7**, 052001 (2023).

[8] A. Cooper, J. P. Covey, I. S. Madjarov, S. G. Porsev, M. S. Safronova, and M. Endres, Alkaline-earth atoms in optical tweezers, Phys. Rev. X **8**, 041055 (2018).

[9] S. Saskin, J. T. Wilson, B. Grinkemeyer, and J. D. Thompson, Narrow-line cooling and imaging of ytterbium atoms in an optical tweezer array, Phys. Rev. Lett. **122**, 143002 (2019).

[10] J. P. Covey, I. S. Madjarov, A. Cooper, and M. Endres, 2000-times repeated imaging of strontium atoms in clock-magic tweezer arrays, Phys. Rev. Lett. **122**, 173201 (2019).

[11] A. Jenkins, J. W. Lis, A. Senoo, W. F. McGrew, and A. M. Kaufman, Ytterbium nuclear-spin qubits in an optical tweezer array, Phys. Rev. X **12**, 021027 (2022).

[12] J. T. Wilson, S. Saskin, Y. Meng, S. Ma, R. Dilip, A. P. Burgers, and J. D. Thompson, Trapping alkaline earth Rydberg atoms optical tweezer arrays, Phys. Rev. Lett. **128**, 033201 (2022).

[13] Y. Wu, S. Kolkowitz, S. Puri, and J. D. Thompson, Erasure conversion for fault-tolerant quantum computing in alkaline earth Rydberg atom arrays, Nat. Commun. **13**, 4657 (2022).

[14] J. W. Lis, A. Senoo, W. F. McGrew, F. Rönchen, A. Jenkins, and A. M. Kaufman, Midcircuit operations using the *omg* architecture in neutral atom arrays, Phys. Rev. X **13**, 041035 (2023).

[15] S. Ma, G. Liu, P. Peng, B. Zhang, S. Jandura, J. Claes, A. P. Burgers, G. Pupillo, S. Puri, and J. D. Thompson, High-fidelity gates and mid-circuit erasure conversion in an atomic qubit, Nature (London) **622**, 279 (2023).

[16] M. Peper, Y. Li, D. Y. Knapp, M. Bileska, S. Ma, G. Liu, P. Peng, B. Zhang, S. P. Horvath, A. P. Burgers, and J. D. Thompson, Spectroscopy and modeling of ^{171}Yb Rydberg states for high-fidelity two-qubit gates, Phys. Rev. X **15**, 011009 (2025).

[17] R. B.-S. Tsai, X. Sun, A. L. Shaw, R. Finkelstein, and M. Endres, Benchmarking and fidelity response theory of high-fidelity Rydberg entangling gates, PRX Quantum **6**, 010331 (2025).

[18] A. Senoo, A. Baumgärtner, J. W. Lis, G. M. Vaidya, Z. Zeng, G. Giudici, H. Pichler, and A. M. Kaufman, High-fidelity entanglement and coherent multi-qubit mapping in an atom array, arXiv:2506.13632 [Nat. Phys. (to be published)].

[19] D. Bloch, B. Hofer, S. R. Cohen, A. Browaeys, and I. Ferrier-Barbut, Trapping and imaging single dysprosium atoms in optical tweezer arrays, Phys. Rev. Lett. **131**, 203401 (2023).

[20] D. S. Grün, S. J. M. White, A. Ortu, A. Di Carli, H. Edri, M. Lepers, M. J. Mark, and F. Ferlaino, Optical tweezer arrays of erbium atoms, Phys. Rev. Lett. **133**, 223402 (2024).

[21] D. S. Grün, L. Bellinato Giacomelli, A. Tashchilina, R. Donofrio, F. Borchers, T. Bland, M. J. Mark, and F. Ferlaino, Light-assisted collisions in tweezer-trapped lanthanides Phys. Rev. Res. **8**, 023067 (2026).

[22] L. Su, A. Douglas, M. Szurek, A. H. Hébert, A. Krahn, R. Groth, G. A. Phelps, O. Marković, and M. Greiner, Fast single atom imaging for optical lattice arrays, Nat. Commun. **16**, 1017 (2025).

[23] G. Biagioni, B. Hofer, N. Bonvalet, D. Bloch, A. Browaeys, and I. Ferrier-Barbut, Narrowline cooling of dysprosium atoms in an optical tweezer array, Phys. Rev. A **112**, 013316 (2025).

[24] A. Patscheider, B. Yang, G. Natale, D. Petter, L. Chomaz, M. J. Mark, G. Hovhannesyan, M. Lepers, and F. Ferlaino, Observation of a narrow inner-shell orbital transition in atomic erbium at 1299 nm, Phys. Rev. Res. **3**, 033256 (2021).

[25] N. Petersen, M. Trümper, and P. Windpassinger, Spectroscopy of the 1001-nm transition in atomic dysprosium, Phys. Rev. A **101**, 042502 (2020).

[26] E. O. Kiktenko, A. S. Nikolaeva, P. Xu, G. V. Shlyapnikov, and A. K. Fedorov, Scalable quantum computing with qudits on a graph, Phys. Rev. A **101**, 022304 (2020).

[27] D. González-Cuadra, T. V. Zache, J. Carrasco, B. Kraus, and P. Zoller, Hardware efficient quantum simulation of non-Abelian gauge theories with qudits on Rydberg platforms, Phys. Rev. Lett. **129**, 160501 (2022).

[28] M. Saffman and K. Mølmer, Scaling the neutral-atom Rydberg gate quantum computer by collective encoding in holmium atoms, Phys. Rev. A **78**, 012336 (2008).

[29] A. Kruckenhauser, M. Yuan, H. Zheng, M. Mamaev, P. Zeng, X. Mao, Q. Xu, T. V. Zache, L. Jiang, R. van Bijnen, and P. Zoller, Dark spin-cat states as biased qubits, Phys. Rev. Lett. **135**, 020601 (2025).

[30] L. Du, P. Barral, M. Cantara, J. de Hond, Y.-K. Lu, and W. Ketterle, Atomic physics on a 50-nm scale: Realization of a bilayer system of dipolar atoms, Science **384**, 546 (2024).

[31] A. L. Shaw, P. Scholl, R. Finkelstein, R. B.-S. Tsai, J. Choi, and M. Endres, Erasure cooling, control, and hyperentanglement of motion in optical tweezers, Science **388**, 845 (2025).

[32] D. González-Cuadra, D. Bluvstein, M. Kalinowski, R. Kaubruegger, N. Maskara, P. Naldesi, T. V. Zache, A. M. Kaufman, M. D. Lukin, H. Pichler, B. Vermersch, J. Ye, and P. Zoller, Fermionic quantum processing with programmable neutral atom arrays, Proc. Natl. Acad. Sci. USA **120**, e2304294120 (2023).

[33] A. Trautmann, M. J. Mark, P. Ilzhöfer, H. Edri, A. E. Arrach, J. G. Maloberti, C. H. Greene, F. Robicheaux, and F. Ferlaino, Spectroscopy of Rydberg states in erbium using electromagnetically induced transparency, Phys. Rev. Res. **3**, 033165 (2021).

[34] D. Studer, P. Dyrauf, P. Naubereit, R. Heinke, and K. Wendt, Resonance ionization spectroscopy in dysprosium: Excitation scheme development and re-determination of the first ionization potential, Hyperfine Interact. **238**, 8 (2017).

[35] The three-dimensional magneto-optical trap is loaded by a slow atomic beam outsourced from a two-dimensional MOT that provides also the vertical beams of the three-dimensional MOT, while the horizontal beams are provided by an independent laser. Optimal operation of the system is thus obtained for slightly different frequencies of the two lasers.

[36] S. H. Youn, M. Lu, U. Ray, and B. L. Lev, Dysprosium magneto-optical traps, Phys. Rev. A **82**, 043425 (2010).

[37] Toptica, model No. DLC TA-SHG PRO, softly focused to a 1-mm waist and nearly 280 mW power on the atoms.

[38] J. Hostetter, J. D. Pritchard, J. E. Lawler, and M. Saffman, Measurement of holmium Rydberg series through magneto-optical trap depletion spectroscopy, Phys. Rev. A **91**, 012507 (2015).

[39] L. Couturier, I. Nosske, F. Hu, C. Tan, C. Qiao, Y. H. Jiang, P. Chen, and M. Weidemüller, Measurement of the strontium triplet Rydberg series by depletion spectroscopy of ultracold atoms, Phys. Rev. A **99**, 022503 (2019).

[40] High Finesse WS8-2.

[41] The absolute uncertainty characterizing the determination of the Rydberg levels is given by the wavemeter precision, the uncertainty with which we can locate the depletion peak, and the possible drift of the MOT laser during the spectroscopy campaign. The first and second terms are stochastic and independent errors and combine into an overall contribution of around 10 MHz. The latter term is again of the order of 10 MHz, but because of its systematic origin, characterized by a rectangular distribution, needs to be simply added to the rest, bringing the total uncertainty to 20 MHz.

[42] See Supplemental Material at http://link.aps.org/supplemental/10.1103/h4q7-6t3s for table.

[43] U. Fano, C. E. Theodosiou, and J. L. Dehmer, Electron-optical properties of atomic fields, Rev. Mod. Phys. **48**, 49 (1976).

[44] G. Nave and U. Griesmann, New energy levels and classifications of spectral lines from neutral and singly-ionized dysprosium (Dy I and Dy II), Phys. Scr. **62**, 463 (2000).

[45] M. Aymar, C. H. Greene, and E. Luc-Koenig, Multichannel Rydberg spectroscopy of complex atoms, Rev. Mod. Phys. **68**, 1015 (1996).

[46] Data from the MQDT fits are available at https//doi.org/10.4231/SN8W-CN80.

[47] There are two aspects of particular difficulty. The first is that there are many lines below $-85\ \mathrm{cm}^{-1}$ which could not be definitively classified but belong to either $J = 9$ or $J = 10$. Below this energy, there is a near degeneracy of one of the quantum defects of $J = 9$ with that of $J = 10$, at the value $\delta \simeq 0.74$, leading to pairs of close levels. The second main difficulty is that the signs of the $V_{i,\alpha}$ are not well defined. Arbitrarily, we set the values of the $V_{i,\alpha}$ to be positive when they are not consistent with zero.

[48] The excitation from the ground state to a Rydberg level may results in trap loss due to a combination of effects, as discussed in Ref. [52] for the Rb case. An atom excited to a Rydberg level can exit the cooling and trapping cycle because it can, with some probability, decay back into some metastable level and fall outside the trapping region before going back to the real ground state. Alternatively, the Rydberg atom can migrate into neighboring higher-l levels with longer radiative lifetimes [53] and again leave the trap before being recycled, or be ionized by either a blackbody or a laser photon. Other processes like Rydberg-Rydberg collisions may also be possible but are supposed to play a minor role.

[49] K.-L. Pham, T. F. Gallagher, P. Pillet, S. Lepoutre, and P. Cheinet, Coherent light shift on alkaline-earth Rydberg atoms from isolated core excitation without autoionization, PRX Quantum **3**, 020327 (2022).

[50] B. Ravon, P. Méhaignerie, Y. Machu, A. D. Hernández, M. Favier, J. M. Raimond, M. Brune, and C. Sayrin, Array of individual circular Rydberg atoms trapped in optical tweezers, Phys. Rev. Lett. **131**, 093401 (2023).

[51] P. Camus, T. F. Gallagher, J.-M. Lecomte, P. Pillet, L. Pruvost, and J. Boulmer, Observation of an electronic correlation for double-Rydberg states of barium, Phys. Rev. Lett. **62**, 2365 (1989).

[52] J. O. Day, E. Brekke, and T. G. Walker, Dynamics of low-density ultracold Rydberg gases, Phys. Rev. A **77**, 052712 (2008).

[53] S. K. Dutta, D. Feldbaum, A. Walz-Flannigan, J. R. Guest, and G. Raithel, High-angular-momentum states in cold Rydberg gases, Phys. Rev. Lett. **86**, 3993 (2001).